Available online at www.sciencedirect.com
ScienceDirect
Cement & Concrete Composites 28 (2006) 914–927
Cement & Concrete Composites
www.elsevier.com/locate/cemconcomp

Deformation capacity of RC piers wrapped by new fiber-reinforced polymer with large fracture strain

Dhannyanto Anggawidjaja [a], Tamon Ueda [a,*], Jianguo Dai [b], Hiroshi Nakai [c]

[a] Division of Built Environment, Hokkaido University, Kita 13 Nishi 8, Kita-ku, Sapporo, Japan
[b] Life Cycle Management Center, Port and Airport Research Institute, Yokosuka 239-0826, Japan
[c] Department of Civil Engineering Design, Mitsui-Sumitomo Construction Co. Ltd., Shinjuku-ku, Tokyo, Japan

Available online 25 September 2006

Abstract

One of the major drawbacks of structure strengthening by fiber reinforced polymer wrapping using materials such as CFRP and AFRP, whose strength and stiffness are high, is the brittle nature of failure mode, which is caused by fracture of the fiber due to low fracturing strain. A series of experiments were conducted to investigate the efficiency of using two new types of fibers, polyethylene naphthalate (PEN) and polyethylene terephthalate (PET) fiber, for seismic strengthening of RC piers. These fibers have the properties of low stiffness and high fracturing strain. Specimens strengthened by PET and PEN fiber sheets wrapping showed considerable improvement in shear capacity and ductility compared to the control specimen. Both PET and PEN showed no tendency to fiber breakage before the predefined ultimate deformation. Pier behaviors such as shear deformation and strain development in both fiber and steel shear reinforcement, and the piers, ultimate failure modes, were carefully examined. Shear deformation increases rather rapidly after peak load and concrete shear capacity decreases with the increase in shear deformation. Stiffness of fiber affects the development of shear deformation and the descending branch of the load–deformation curve after the peak load. A simple model to predict the piers deformation capacity, based on the experimental results, was proposed.

Keywords: Shear; Ductility; Wrapping; PET; PEN; High fracturing strain

1. Introduction

The recent large earthquakes in Japan exposed the vulnerabilities of its existing reinforced concrete structures. The Great Hanshin earthquake revealed that structures designed by the old design code need strengthening of their shear capacity. Furthermore, in the structures with comparatively high shear capacity, it was also noted that increased ductility in order to withstand large seismic action is necessary.

Strengthening of reinforced concrete piers with fiber material jacketing has proven to be able to meet these two demands efficiently. The usage of fiber material in the strengthening scheme is preferable to steel in many cases [1–4] due to the advantages of fiber compared to steel [5,6]. The high strength-to-weight ratio of fiber, resistance to corrosion and easy handling and installation make fiber reinforced polymer (FRP) jackets the preferred material for strengthening.

Due to the above-mentioned advantages, conventional FRP materials such as aramid, carbon, and glass are frequently used for seismic strengthening of reinforced concrete piers. Many researchers have proven the effectiveness of their application in shear and ductility enhancement. However, it should be noted that due to their low fracturing strain capacity, these fiber materials tend to fail sooner due to fiber breakage before the structures can fully utilize their reinforced strength [3,7]. The breakage of fiber causes a loss of confinement and a sudden loss of load-carrying

* Corresponding author. Tel.: +81 11 706 6218; fax: +81 11 706 6582.
E-mail addresses: dhannyanto@yahoo.com (D. Anggawidjaja), ueda@eng.hokudai.ac.jp (T. Ueda), dai@pari.go.jp (J. Dai), hironky2@smcon.co.jp (H. Nakai).

0958-9465/$ - see front matter © 2006 Elsevier Ltd. All rights reserved.
doi:10.1016/j.cemconcomp.2006.07.011

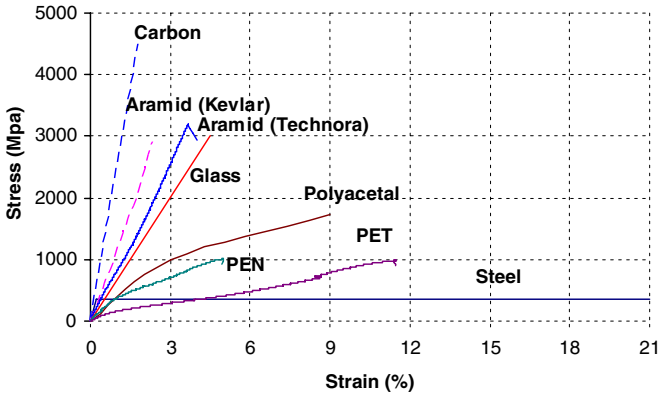

Fig. 1. Stress and strain relationships of various materials.

capacity and directly limits the ductility potential. Because this can lead to sudden failure of the structure, breakage of fiber is not favourable. In the design procedure the limitation of fiber strain is used to determine the reinforced concrete (RC) piers strength capacity to avoid rupture of fiber material [8].

New fiber materials such as polyacetal fiber (PAF), polyethylene naphthalate (PEN) and polyethylene terephthalate (PET) have properties of large fracturing strain and low stiffness in comparison to aramid, carbon, and glass fibers [9–11]. Fig. 1 shows the stress–strain relationships of various fiber materials. Previous studies [9] using polyacetal fiber showed that large fracturing strain fiber is less likely to fracture before the RC piers reach their ultimate deformation. Continuous shear force and enhanced ductility could be gained from the fiber to compensate for the reduction concrete shear capacity due to damage induced by large cracks and seismic action.

The objective of this research is to investigate the shear strengthening and ductility enhancement of reinforced concrete piers confined with high fracturing strain fiber materials, PET and PEN. Based on these test results, models for predicting the ultimate deformation of strengthened RC piers are proposed.

2. Experimental program

2.1. Details of test setup

A total of 15 RC piers in four experimental batches were constructed to represent a rectangular pier of a regular bridge, while the bottom part represented the footing of the pier. The first and second batch specimens were rectangular piers with a cross section of 400×400 mm. The third and fourth batches were rectangular piers with dimensions of 600×600 mm. The pier cross section areas of third and fourth batches were enlarged to give closer resemblance and response to actual pier dimensions. The size effect was not considered as a parameter in this research. All pier corners were rounded with a rounding radius of 25 mm.

Table 1
Specimens details

Specimen	f'_c	a/d	ρ_t (%)	ρ_w (%)	ρ_f (%)	Fiber material
First batch						
SP1	29.5	3	2.87	0.16	–	–
SP2	29.5	3	2.87	0.16	0.13	A2
SP3	29.5	3	2.87	0.16	0.38	PEN
SP4	29.5	3	2.87	0.16	0.37	PET
Second batch						
SP5	31.7	3	2.87	0.16	0.19	PET
SP6	31.7	4	2.87	0.16	0.12	PET
SP7	31.7	4	2.87	0.16	0.06	PET
SP8	31.7	4	2.87	0.16	–	
SP9	31.7	4	3.59	0.16	0.12	PET
SP10	31.7	4	2.15	0.16	0.06	PET
Third batch						
SP11	31.7	4	2.82	0.2	0.25	PET
SP12	31.7	4	2.82	0.2	0.125	PET
Fourth batch						
SP13	34.5	3	2.82	0.2	0.29	PET
SP14	23.7	3	2.82	0.09	0.42	PET
SP15	31.1	3	2.82	0.09	0.42	PEN

Table 2
Shear capacities

Specimen	V_c (kN)	V_s (kN)	V_{tot} (kN)	M_u (kN m)	V_u (kN)	V_{tot}/V_u	Ductility
First batch							
SP1	151	79	230	331	288	0.8	5.09
SP2	151	79	230	331	288	0.8	11.84
SP3	151	79	230	331	288	0.8	10.65
SP4	151	79	230	331	288	0.8	11.42
Second batch							
SP5	155	79	234	334	290	0.8	7.98
SP6	155	79	234	334	223	1.05	9.05
SP7	155	79	234	334	223	1.05	8.46
SP8	155	79	234	334	223	1.05	7.40
SP9	169	79	248	401	267	0.93	8.76
SP10	151	79	230	265	177	1.3	10.41
Third batch							
SP11	318	206	524	1018	463	1.13	8.52
SP12	318	206	524	1018	463	1.13	7.54
Fourth batch							
SP13	327	105	432	1051	637	0.84	7.76
SP14	289	83	372	1010	612	0.61	4.12
SP15	316	83	399	1058	641	0.62	6.87

Tables 1 and 2 give details of the test specimens. The first and second batch specimens used 19 mm deformed bars for longitudinal reinforcement and 6 mm deformed bars for stirrups. The third batch specimens used 25 mm deformed bars for longitudinal reinforcement and 10 mm deformed bars for stirrups. The fourth batch specimens used 25 mm deformed bars with differing shear reinforcement ratios. SP13 of the fourth batch used 10 mm deformed bars for stirrups, while SP14 and SP15 of the fourth batch used 6 mm deformed bars for stirrups. The longitudinal reinforcements in the piers were extended into

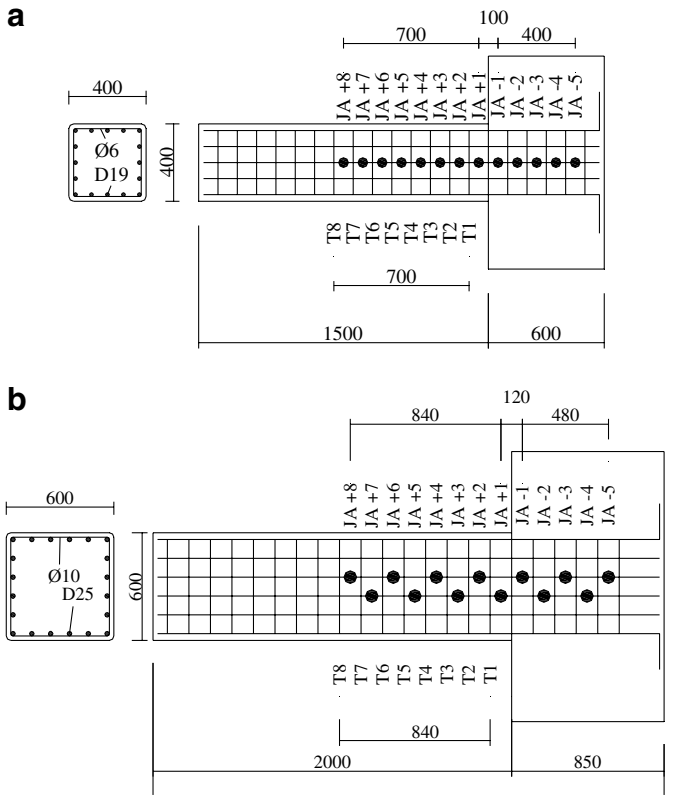

Fig. 2. Arrangement of reinforcements. (a) 400×400 mm specimen, (b) 600×600 mm specimen.

the footing. Details of the reinforcement arrangement are shown in Fig. 2.

Fiber wrapping in the specimens was done in two parts of the piers. Aramid (A2), PEN and PET fibers were used to wrap the plastic hinge area. Details of the fiber material used for plastic hinge area are listed in Table 1. The plastic hinge area is considered as area $1.0D$ for the first and second batch specimens and $1.5D$ for the third and fourth batch specimens from the face of the footing, where D is the section depth of the rectangular pier. High stiffness fiber material wrapping using Aramid (Kevlar) was applied to the area beyond the plastic hinge. This measure was taken to ensure that the failure of the strengthened specimens would be concentrated at the plastic hinge area and to observe the effectiveness of the respective fibers.

The first batch was carried out in order to verify the effectiveness of the new fiber materials, PEN and PET, in shear strengthening and ductility enhancement for shear capacity-deficient piers, compared to that of Aramid (A2) fiber. The aim was to achieve a ductility ratio, which is the ratio of ultimate deformation to yield deformation, at an ultimate state greater than 10, according to JSCE recommendations [12]. The first batch consisted of four specimens: a control specimen and three specimens strengthened with three different fiber materials, AFRP, PEN and PET, respectively. The tensile capacity of the fiber materials was kept the same in all three cases. Each specimen had rectangular pier dimensions of $400 \times 400 \times 1500$ mm and footing dimensions of $1100 \times 600 \times 1050$ mm.

The second batch was carried out in continuity with the previous batch in order to determine the effects of fiber volumetric ratio and shear strength ratio on ductility performance. It consisted of six specimens: a control specimen and five PET-strengthened specimens with different ratios of PET fiber and shear strength to flexural strength. Each specimen had rectangular pier dimensions of $400 \times 400 \times 1850$ mm and footing dimensions of $1100 \times 600 \times 700$ mm.

The third batch was carried out in continuity with the second batch, with larger pier and footing dimensions and different fiber ratios. This batch consisted of two specimens with different fiber ratios. Each specimen had rectangular pier dimensions of $600 \times 600 \times 2400$ mm and footing dimensions of $1500 \times 1500 \times 850$ mm.

The fourth batch was carried out for the purpose of investigating the effects of replacing steel shear reinforcement with PEN and PET fiber material. It consisted of three specimens, each having rectangular pier dimensions of $600 \times 600 \times 2000$ mm and footing dimensions of $1500 \times 1500 \times 850$ mm.

2.2. Material properties

The specimens within the same batch were cast together with one batch of concrete. Each batch of the concrete was tested to obtain the concrete's compressive strength. Steel reinforcements consisted of tie reinforcements and longitudinal reinforcements. Both reinforcements were tested to find the stress–strain relation. Table 3 shows the properties of the steel reinforcements used in this experiment.

Four types of fiber were used in the experiment. Aramid (Kevlar) material was used to strengthen the area beyond the plastic hinge area for all strengthened specimens. A2,

Table 3
Properties of steel reinforcement

Item	Sp 1–10	Sp 11–12	Sp 13	Sp 14–15
Longitudinal reinforcement	D19	D25	D25	D25
Yield strength (N/mm^2)	394	370.9	388.2	388.2
Young modulus (N/mm^2)	1.76E + 05	1.83E + 05	1.94E + 05	1.94E + 05
Shear reinforcement	D6	D10	D10	D6
Yield strength (N/mm^2)	382.8	361.4	361.4	328
Young modulus (N/mm^2)	1.91E + 05	1.85E + 05	1.92E + 05	1.64E + 05

Table 4
Properties of fiber materials

Item	Aramid Kevlar (A1)	Aramid Teknora (A2)	PET	PEN
Ultimate strength (N/mm^2)	2670	3246	923	1028
Ultimate strain	0.022	0.041	0.138	0.045
Young modulus (N/mm^2)	1.22E + 05	7.95E + 04	6.70E + 03	2.26E + 04

PEN and PET fibers were used to strengthen the plastic hinge area (Table 1). Table 4 shows the properties of the fiber materials used in this experiment.

2.3. Instrumentation and testing procedure

All specimens were well instrumented during testing to monitor load, deflection at the loading point, and strains at several locations. Three transducers (LVDT) were mounted on rigid steel frames to measure lateral displacement of piers. The loading devices are shown in Fig. 3. Five LVDTs were mounted on the plastic hinge area to measure the shear deformation (Fig. 4). Two LVDTs were mounted directly atop the pier to measure pier base rotation. Four LVDTs were mounted at the pier base to measure horizontal slip and rotation of the base. Strain gauges were used to measure the strain development in the flexural reinforcements, shear reinforcements and fiber confinements. Strain gauges to measure longitudinal reinforcement strain were mounted on the longitudinal reinforcements located at the middle of each flexural side. All shear reinforcements had strain gauges mounted at the center of each shear side. Fiber strain was measured by extensive application of strain gauges at the plastic hinge area for all flexural and shear sides.

The specimens were subjected to a combination of cyclic horizontal load and constant axial load. A compressive vertical load equal to 1.0 MPa, representing the dead load of the superstructure, was applied. Displacement at the loading point of the specimens, when longitudinal reinforcement at the bottom of the pier yielded, was considered

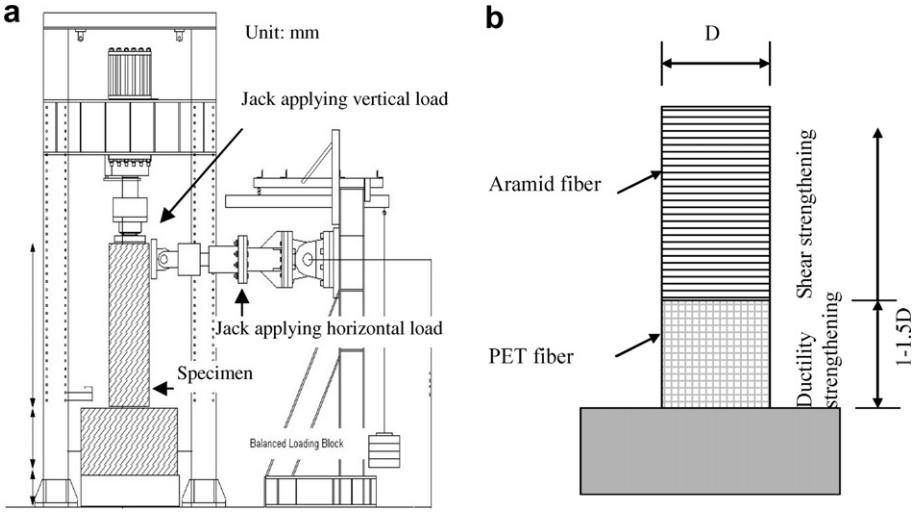

Fig. 3. Experimental setup. (a) Loading devices, (b) strengthening scheme.

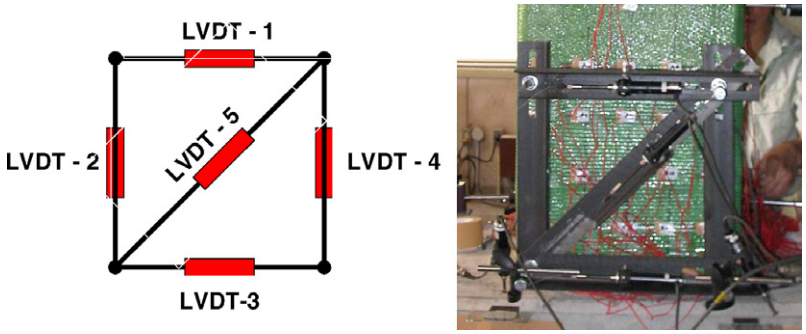

Fig. 4. Measurement for shear deformation.

as *flexural yielding displacement* (δ_y), and the corresponding load was *yielding load* (P_y). Horizontal cyclic load was applied gradually in increments of $1.0\delta_y$ for each cycle, consisting of push/pull loading conditions until the pier was unable to sustain the applied load. The ultimate deformation was defined as the displacement amplitude when the applied load dropped to the yielding load under either push or pull loading conditions.

3. Experimental results and discussion

3.1. General description

In the first-batch specimens, the control specimen (SP1) showed brittle shear failure. Shear reinforcement yielding occurred at $-1\delta_y$, and extensive diagonal shear crack occurred in the specimen at $2\delta_y$, which caused a loss of specimen load-carrying capacity. SP1 was able to develop a ductility ratio of 5.09 at the ultimate state. Other specimens that were strengthened using fiber wrapping showed ductile shear failure. A typical characteristic of ductile shear failure was that, after the peak load was achieved, a decrease of load occurred gradually due to widening of the flexural shear crack, which caused a decrease in the concrete contribution. Although the specimens were initially designed as piers with insufficient shear capacity, the fiber confinement was able to provide additional shear capacity and allowed the specimens to develop their plastic flexural strength. All strengthened specimens were able to develop the ductility ratio greater than $10\delta_y$ (see Table 2 and Fig. 5): SP2, SP3 and SP4 developed ductility ratios of 11.84, 10.65 and 11.42, respectively. Initial yielding of the shear reinforcement occurred at $3\delta_y$ and yielding of all shear reinforcements in the plastic hinge area occurred at $5\delta_y$, followed by buckling of the longitudinal reinforcement at $6\delta_y$. Buckling was indicated by bulging of the cover concrete through the fiber sheet at the plastic hinge area. The fiber in the strengthened specimens showed no breakage, with the largest strain development for SP2, SP3 and SP4 recorded at 23 120μ, 23 270μ and 30 460μ, respectively. SP5 of the second batch was compared to SP4 of the first batch. Due to the lesser amount of fiber, SP5 showed ductile shear failure with larger strain development (45 320μ) compared to SP4, which resulted in a smaller ductility ratio of 7.98. Aramid fiber wrapping above the plastic hinge area of SP5 ruptured while PET fiber in the plastic hinge zone showed no breakage due to the large fracturing strain of PET.

The second and third batch specimens (SP6–SP12) demonstrated flexural failure. A typical characteristic of flexural failure was that after peak load was reached,

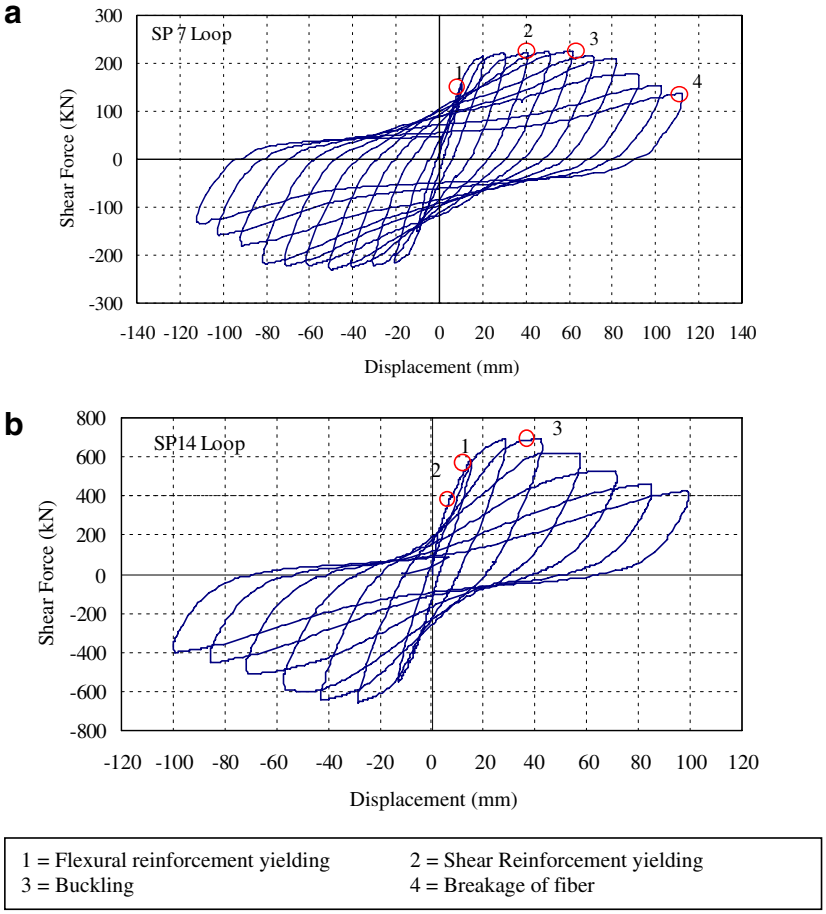

Fig. 5. Load–displacement hysteretic loops. (a) Flexural failure, (b) ductile shear failure.

specimens were able to maintain it until the shear reinforcement yielded. As the shear reinforcement yielded, it was followed by buckling, which indicated the commencement of member failure. In the control specimen (SP8), yielding of all shear reinforcements occurred at $5\delta_y$, followed by buckling of longitudinal reinforcements at $6\delta_y$ when load-carrying capacity suddenly dropped. The strengthened specimens showed a slower decline in load-carrying capacity after yielding of the shear reinforcement. The ductility ratio at the ultimate state for the strengthened specimens was presented in Table 2. Breakage of PET fiber was observed, after the ultimate state, at the corner of the specimen in SP7, SP9, SP10, SP11 and SP12. Breakage of PET occurred in SP7 at $11\delta_y$ with a recorded strain value of 11%, in SP9 at $11\delta_y$ with a recorded strain value of 13% and in Sp10 at $13\delta_y$ with a recorded strain value of 9.5%. SP11 and SP12 showed breakage of PET fiber; however, strain values could not be measured since the strain gauges were already broken. Damages to the specimens can be seen in Fig. 6.

The fourth batch specimens revealed ductile shear failure. In SP13, shear reinforcement yielding occured at $2\delta_y$; however, buckling was not immediately observed. It is assumed that buckling was delayed due to the large amount of fiber used for confinement. Buckling occurred at $7\delta_y$. In SP14 and SP15, shear reinforcement yielding occured before the flexural reinforcement yielded. The fiber confinement was able to provide additional shear capacity and allowed the specimens to develop their plastic flexural strength. Both SP14 and SP15 reached peak load $2\delta_y$ before the load-carrying capacity began to decrease. Buckling of the flexural reinforcement occurred at $4\delta_y$ and caused a more severe decrease in load carrying capacity. No fiber breakage was observed for this batch.

Debonding of fiber was observed in all specimens. Before the debonding occurred, the strain gauge that was intersected by the shear crack line showed the greatest value of strain. The debonding of the fiber occurred gradually, starting from the shear crack line and extending in a lateral direction. After debonding occurred, the strain gauges showed fairly similar values. The experimental results showed that fiber in the crack line area will start to debond once the strain reaches 4000 μm. The debonding of the fiber from the concrete surface resulted in a lower fiber contribution to shear capacity. This subject will be covered in detail in Section 3.3.

Two failure modes were observed for all strengthened specimens: flexural failure and ductile shear failure (Fig. 5). Flexural failure occurs when the column develops its plastic flexural strength followed by yielding of the steel shear reinforcements. Due to yielding of the steel shear reinforcement, the stiffness of the confinement decreases. Decreased confinement together with load reversal causes a decrease in load carrying capacity of the concrete. Inadequate lateral support from the transverse reinforcements also allows the longitudinal reinforcements to buckle. Buckling is the starting point of the descending branch in load–deformation curves. Typical load–deformation hysteretic loops for this failure mode can be seen in Fig. 5(a).

Ductile shear failure occurs when the column develops its plastic flexural strength but ultimately fails in shear. Widening of the flexure-shear crack after flexural reinforcement yielding results in the deterioration of concrete shear capacity due to the loss of aggregate interlocking. Stiffness degradation in the hinge zone also allows further larger shear deformation to occur. A typical load deformation hysteretic loop for this failure mode can be seen in Fig. 5(b).

3.2. *P–δ curves*

As shown in Fig. 7, SP2–SP4 showed ultimate ductility ratios greater than 10 despite the fact that the reference specimen SP1, whose shear strength ratio was less than 1.0, showed a much smaller ductility ratio. This fact indicates that PET and PEN confinement could provide sufficient shear capacity contribution regardless of their low stiffness. For ductility-enhancement purposes, the application of PET and PEN was also proven to be cost effective compared to aramid fiber: the comparison of the material cost for the aramid, PEN, and PET in this batch was 8:6:3. Based on this result it was decided to use PET as

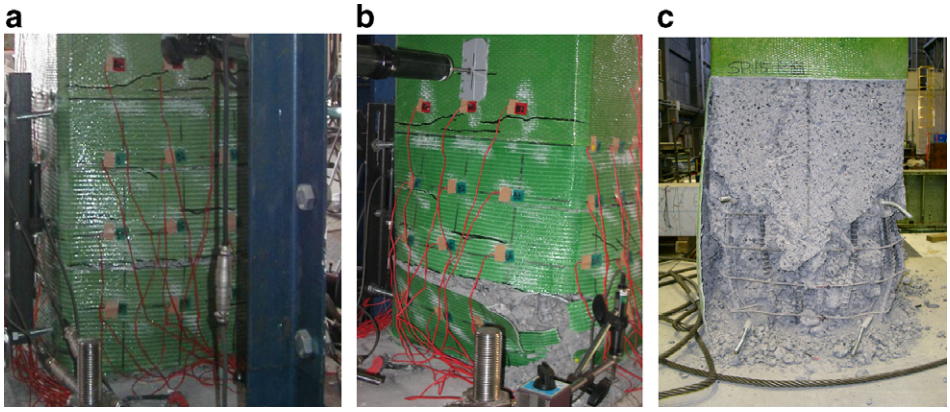

Fig. 6. Damage to specimens. (a) Ultimate state (no breakage), (b) fiber breakage, (c) plastic hinge damage.

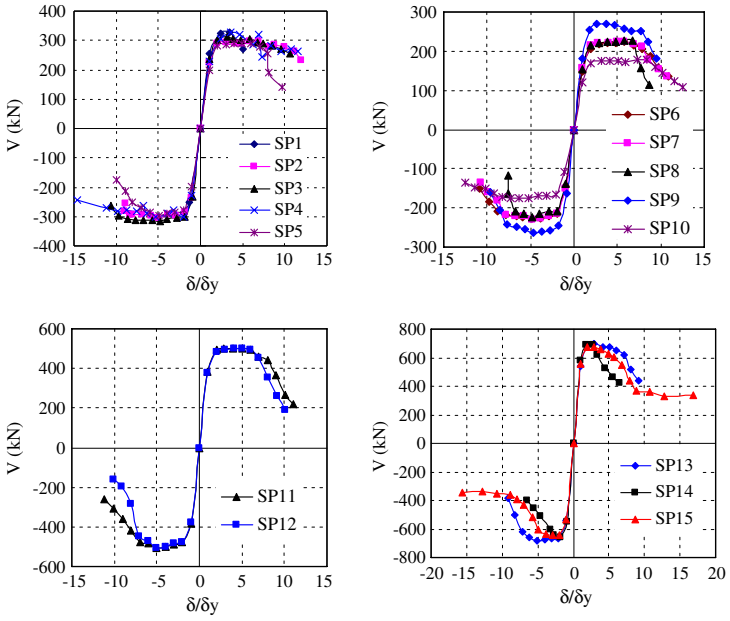

Fig. 7. Load–displacement envelope curves.

the fiber material in the plastic hinge zone for the next batch of experiments.

For specimens with sufficient shear capacity (SP6, SP7, SP8, SP11 and SP12) with shear strength ratios greater than 1.0 before strengthening, the application of PET could enhance ductility. SP6 and SP7, with fiber ratios of 0.12% and 0.06%, respectively, had greater ultimate ductility compared to control specimen SP8. SP11 and SP12 also showed that additional PET confinement gives greater ductility.

The fourth batch specimens were all designed as shear deficient columns (or with shear strength ratios of less than 1.0). In this batch, SP13 was compared to SP14 and SP15. Both SP14 and SP15 had a certain amount of their steel shear reinforcement replaced with PET and PEN fiber, respectively, in order to have the same ductility as SP13, which had more steel shear reinforcement. SP14 and SP15 had the same fiber ratio. As can be seen from Fig. 7, SP15 had greater ductility compared to SP14, and approximately the same ductility as SP13. From the experimental results it is concluded that in the case of a seriously shear-deficient column, high fracturing strain fiber material (PET) can still compensate for the insufficiency of steel shear reinforcement despite its low stiffness; but that a greater amount of fiber is required in comparison with the case of high stiffness fiber material.

3.3. Development of strains in PET sheets and shear reinforcement

The average strain for both steel shear reinforcement and fiber wrapping was calculated taking the average of the strain that developed along the shear crack line. Since all specimen surfaces were covered by fiber, direct observation of the crack line was not possible. The locations of the strain gauges at different heights showing maximum strain were considered to be intersected by the shear crack. The shear crack line was predicted by connecting the location of the strain gauges location at different heights at an early deformation level where debonding of fiber had not occurred.

As mentioned in Section 3.1, debonding occurred when fiber around the shear crack line reached 4000 μm and started to expand in a lateral direction with a rather similar value of strain development. The average strain of fiber along the shear crack line was used in the analysis process before debonding occurred. After debonding occurred, the average strain value of all strain gauges at the plastic hinge area, excluding the strain gauges at the bottom corner of the piers, was used in the analysis process. The strain gauges in the corner were excluded to minimize the effect of strain development due to the confinement effect.

At low deformation levels, steel and fiber tended to show similar strain development for all specimens. Greater fiber strain development was noticed in specimens with ductile shear failure, more so than in specimens with flexural failure according to the experiment results. This showed that fiber provided a larger shear contribution to shear capacity in compensating for the lack of shear capacity in specimens with ductile shear failure, such as SP2–SP4 and SP13–SP15, since those specimens had initial shear strength ratios of less than 1.0. The amount of strain that developed in the fiber also depended on the amount of fiber used. As shown in Fig. 8(a), SP7 showed higher strain development compared to SP6, since less fiber was used in SP7 for strengthening.

At higher deformation levels, different strain development of the shear reinforcement and fiber was observed later in the experiment. The average strain observed in

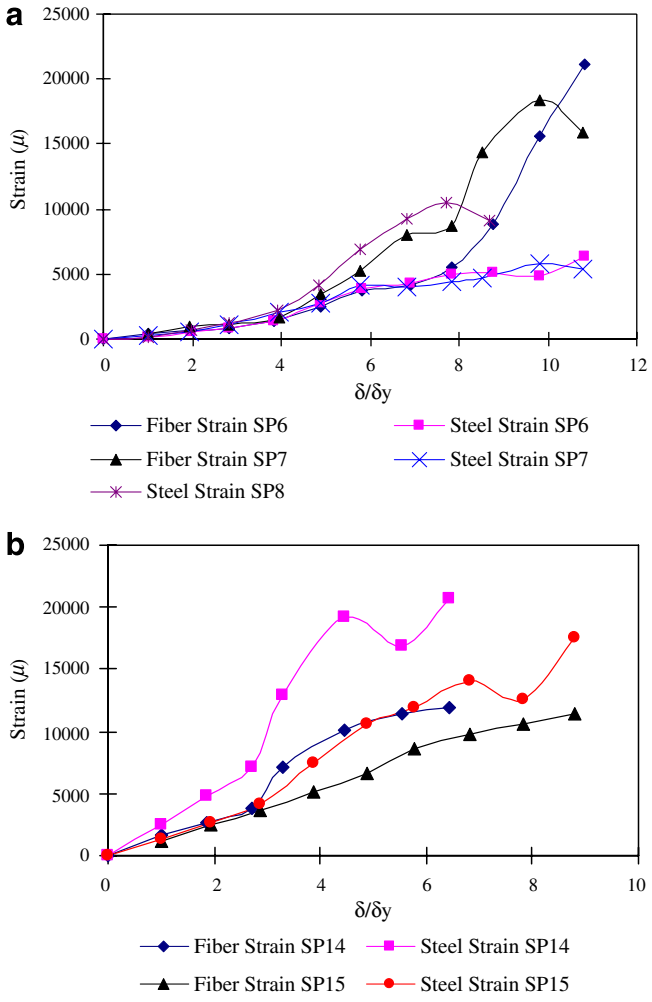

Fig. 8. Fiber and steel strains. (a) Strain development at typical flexural failures, (b) strain development at typical ductile shear failures.

the fiber and steel shear reinforcement is shown in Fig. 8(a) and (b) for specimens with flexural failure and ductile shear failure, respectively. For specimens with flexural failure, PET fiber developed higher average strain compared to steel shear reinforcement at a higher deformation level. The difference was due to the confinement effect of the fiber, which caused high strain development at the corner of the pier. For this reason the strain of fiber at the bottom corner was excluded from the analytical process. In specimens with ductile shear failure, debonding of the fiber from the concrete surface was noticed at a high deformation level. Fiber debonding started at the area around the crack line and propagated to both sides of the crack line. Due to this debonding, the PET fiber showed less strain development than the steel shear reinforcement. In addition, the loss of bonding between the fiber and the concrete caused *A* reduction in the fiber contribution to the shear-resisting mechanism and larger shear crack propagation. As a result, the concrete started to lose its shear contribution, and, in addition, the pier's load carrying capacity was reduced.

When subjected to higher deformation levels, the locations of the maximum strain value were different from those at low deformation levels, especially for specimens with flexural failure. The maximum strain locations were mostly at the corner of the piers. These locations did not show the actual crack line, nor did the corresponding strain show the actual fiber shear contribution. Therefore average fiber strain, excluding the strain in the corner, was used for the analysis since it gave a better representation of the actual shear contribution.

3.4. Deformation components

To understand the seismic performance of RC piers strengthened using PET fiber, it is essential to understand the effect of fiber wrapping on their deformation capability. Many researchers have used fiber modeling to predict the ultimate deformation of RC piers strengthened with conventional FRP materials. The corresponding ultimate state usually depends either on crushing of the concrete or the fracturing strain of FRP; however, these experimental results showed that for RC piers strengthened with PET and PEN, the ultimate state was not governed by FRP fracture as mentioned above. Another aspect is that fiber modeling for flexural deformation has difficulty in dealing with the deformation due to shear and corresponding shear deterioration due to cyclic loading, which produces a ductile shear failure as mentioned above. Fig. 9 shows a typical P–δ curve modeled on the basis of experimental results. In this curve, C is the point where flexural cracking occurs, Y is the yield point, A is the approximate point of displacement at which the maximum load is reached after the yielding point, and M is the point of maximum displacement, where the maximum load is maintained before the decrease of load-carrying capacity. In the case of ductile shear failure specimens, points A and M might be close to each other, or even have the same point, due to shear failure in which specimens cannot utilize their flexural strength. In flexural failure specimens, point M might correspond to the buckling of longitudinal reinforcements or concrete failure due to concrete crushing. Fig. 10 describes these failure modes. The dashed line represents flexural failure and the solid line represents ductile shear failure. In ductile shear failure the RC pier can not fully utilize its flexural

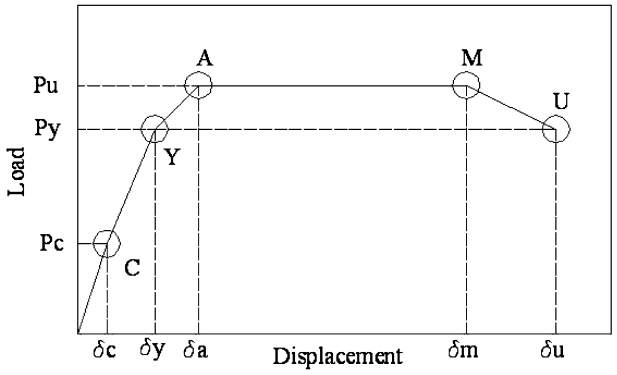

Fig. 9. P–δ curve model.

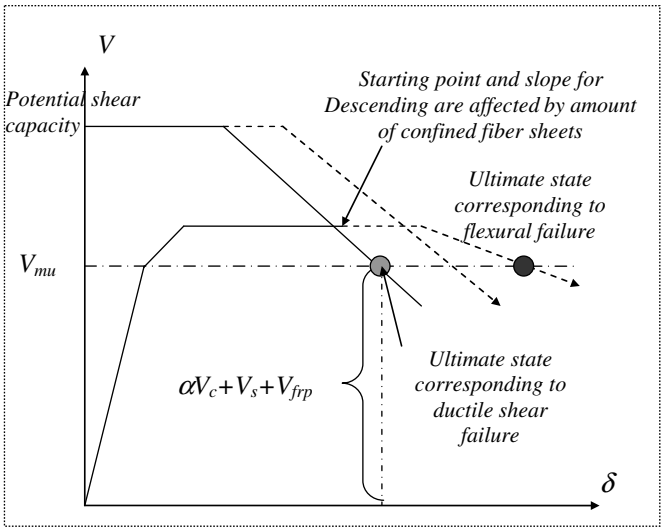

Fig. 10. Failure mode concept.

capacity due to the decrease in shear capacity, and the RC pier fails. The decreasing slope of load-carrying capacity depends on the amount of fiber used for specimen wrapping. Greater fiber strengthening will result in a slower decline in load carrying capacity.

The following sections will experimentally and analytically discuss the deformation components at the characteristic points shown in Fig. 9. The deformation components are separated into deformation due to bending, pullout and shear, as can be seen in Fig. 11. Lastly, an empirical equation was proposed to determine the decreasing slope of load carrying capacity.

3.4.1. Drift ratio due to pullout

Deformation of strengthened RC piers at the loading point due to pullout of the steel reinforcement from the footing can be calculated by the following equations (see Fig. 11):

$$\delta_l = \frac{L \cdot S}{d - x} \tag{1}$$

where

δ_l pullout deformation (cm)

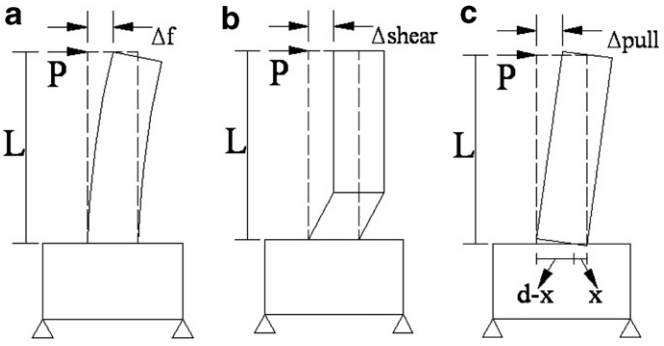

Fig. 11. Deformation components. (a) Flexural deformation; (b) shear deformation; (c) pullout deformation.

S pullout of reinforcement (cm), which can be obtained in experiment by integrating the longitudinal reinforcement strain which occurred in the footing

L shear span (cm)

d effective height of cross section (cm)

x neutral axis depth (cm), which can be obtained by comparing the tensile strain of the longitudinal reinforcement to the compression strain of the longitudinal reinforcement at the opposite side during the experiment

As shown in Fig. 12(a), pullout deformation had a significant effect at a minor displacement level. However with increasing displacement, plastic rotation developed in the

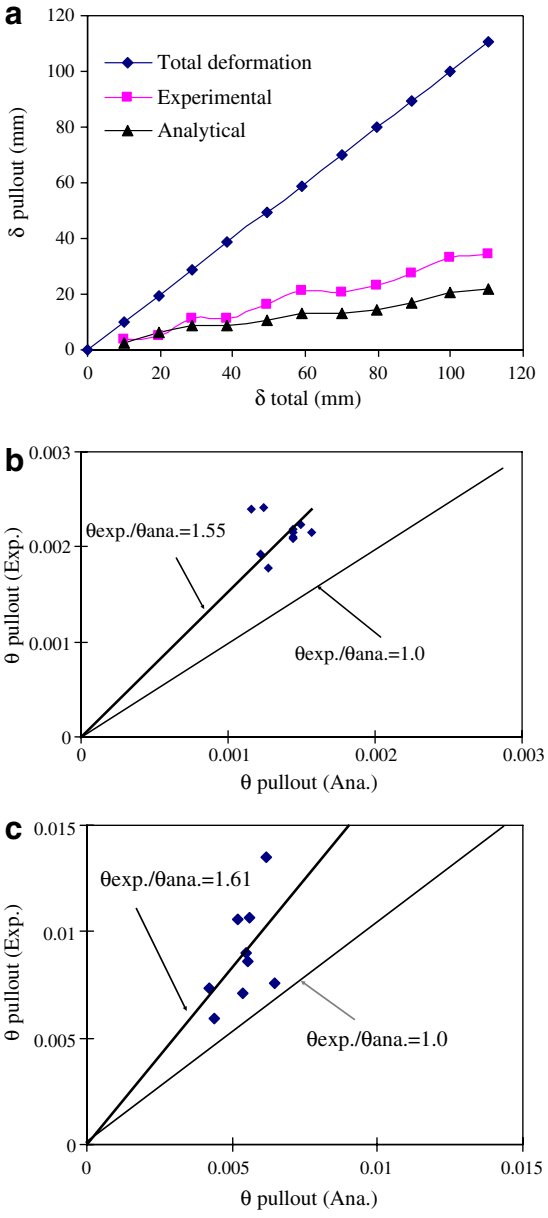

Fig. 12. Pullout drift angle at yield and maximum load. (a) Pullout deformation versus total deformation, (b) drift ratio due to pullout of reinforcement at yielding load, (c) drift ratio due to pullout of reinforcement at maximum load.

plastic hinge and the effect of pullout deformation became less significant. At yielding load and maximum load, pullout deformation of about 30% of total deformation and became ±17% at the ultimate state.

The slip of reinforcement can also be predicted analytically at the yielding load using Eqs. (2) and (3), and after yielding of the longitudinal reinforcement using Eqs. (4) and (5) based on paper by Ishibashi et al. [13]. This analysis method was based on the bond between reinforcement and surrounding concrete proposed by Shima et al. [14]. The equations proposed in these papers are also used in the JSCE code for seismic performance verification [15]. The pullout deformation equations proposed by Ishibayashi et al. for different stages of reinforcement strain are as follows:

Slip of reinforcement at yield strain:

$$S = \frac{7.4\alpha_y \cdot \varepsilon_y(2 + 3500\varepsilon_y)}{f'^{2/3}_{ck}} \cdot \varphi \quad (2)$$

$$\alpha_y = 1 + 0.9e^{0.45\left(1-\frac{C_s}{\varphi}\right)} \quad (3)$$

Slip of reinforcement after yield:

$$S = s \cdot \frac{\varphi}{K \cdot f_c} \quad (4)$$

where s value is different for each strain level of reinforcement.

- When the reinforcement strain takes the value of yield strain (ε_y)

$$s = \varepsilon_y(2 + 3500\varepsilon_y) \cdot \alpha_y \quad (5.1)$$

- When the reinforcement strain is at the initiation point of strain hardening area (ε_{sh})

$$s = 0.5(\varepsilon_{sh} - \varepsilon_y) + s(\varepsilon_y) \quad (5.2)$$

- When the reinforcement strain takes the value at the change in gradient of the non-dimensional slip in the reinforcement strain hardening area (ε_a)

$$s = 0.08(f_u - f_y)(\varepsilon_a - \varepsilon_{sh}) + s(\varepsilon_{sh}) \quad (5.3)$$

$$\varepsilon_a = \varepsilon_{sh} + \left(\frac{0.132 - \frac{s(\varepsilon_y)}{2}}{0.13(f_u - f_y)}\right)$$

- When the reinforcement strain is greater than ε_a

$$s = 0.027(f_u - f_y)(\varepsilon_s - \varepsilon_a) + s(\varepsilon_a) \quad (5.4)$$

where

S	pullout of reinforcement (cm)
s	non-dimensional measure of reinforcement pullout
α_y	effect of bar spacing
φ	diameter of reinforcement bar (cm)
f'_{ck}	strength of footing concrete (N/mm^2)
f_y	yield strength of reinforcement (N/mm^2)
f_u	tensile strength of reinforcement (N/mm^2)
C_s	bar spacing (cm)
ε_y	strain at reinforcement yield
ε_{sh}	strain at initiation of reinforcement strain hardening
ε_a	point of non-dimensional slip gradient change in strain hardening area
ε_s	reinforcement strain

Substituting the slip of reinforcement value in Eq. (3), the deformation of piers due to pullout of reinforcement can be gained analytically and plotted in Fig. 12(a). The comparisons between the experimental results and the analytical results at the yielding load and the maximum load are shown in Fig. 12(b) and (c), respectively. The prediction results are somewhat conservative for both yielding and maximum load levels, but the analysis represents the result nevertheless.

3.4.2. Drift ratio due to shear deformation and deterioration of concrete

The shear deformation was measured using the instruments shown in Fig. 4. With the obtained value of length from five transducers, shear deformation can be calculated using the method proposed by Jaqin et al. [10]. The truss model proposed by Ueda [16] was used as the analytical method.

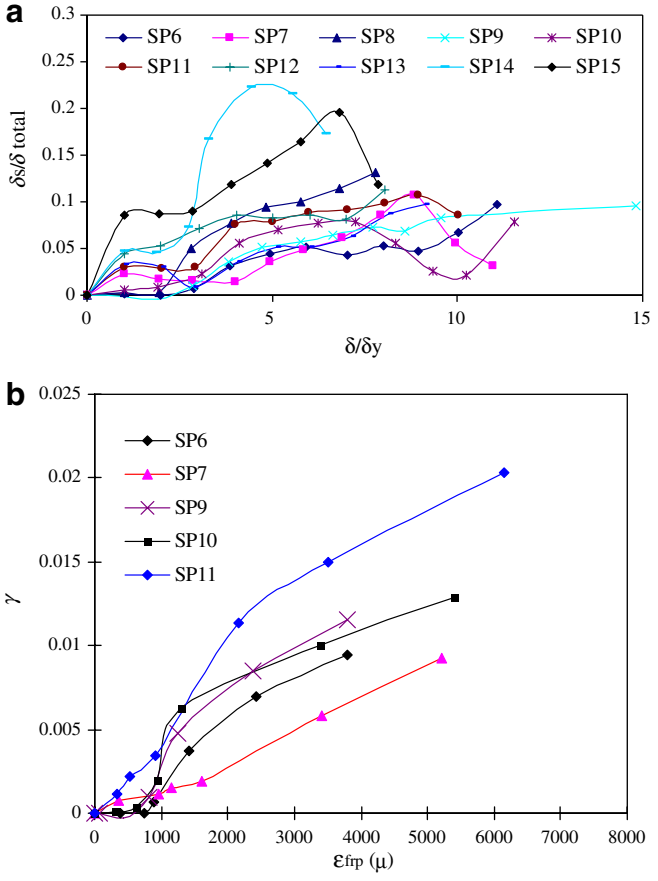

Fig. 13. Shear deformation development. (a) Ductility versus shear deformation ratio to total displacement, (b) transverse reinforcement strain versus shear deformation ratio (γ).

As seen in Fig. 13(a), shear deformation increases its contribution to the total deformation with the increase of displacement amplitude. At the ultimate state, it occupies about 5–12% of the total deformation depending on the shear steel reinforcement ratio and the fiber strengthening ratio. Shear deformation in two specimens, SP14 and SP15, shows much higher values and different tendencies compared to the other specimens in Fig. 13(a). According to experimental observation, this was possibly due to the instability of the test instruments for measuring the shear deformation at the hinge zone for these last two testing specimens. Fig. 13(b) shows the development of shear deformation ratio (γ) with the average strain in FRP sheets. It is indicated that at the same level of strain development in the fiber, greater shear deformation occurs for piers with a high fiber ratio.

Increasing shear deformation causes significant damage to the concrete at the plastic hinge zone and causes it to lose its shear contribution. In the experiment, decrease in the concrete contribution to shear strength was observed with the development of shear strain (γ) (see Fig. 14). In Fig. 14 the shear capacity contributed by concrete is calculated by subtracting the steel and fiber shear reinforcement contribution based on the truss analogy method from the applied shear force. The peak shear capacity of concrete observed during the experiment was higher than that predicted by the JSCE code [12] (see Table 2 and Fig. 14).

As the concrete deteriorated, the shear contributions from the steel reinforcement and the fiber increased to compensate for the loss of shear capacity of the concrete. When the shear steel reinforcement yielded, the fiber started to give a larger contribution to shear capacity, accompanied by fiber elongation. However, the elongation of fiber was also accompanied by the widening of the shear crack; in other words, a more rapid deterioration of concrete shear capacity. In general, the potential shear capacity decreases due to the deterioration of concrete as shown in Fig. 10. When the potential shear capacity of the piers reduces to the level of their potential flexural capacity, the load carrying capacity starts to decrease. Therefore,

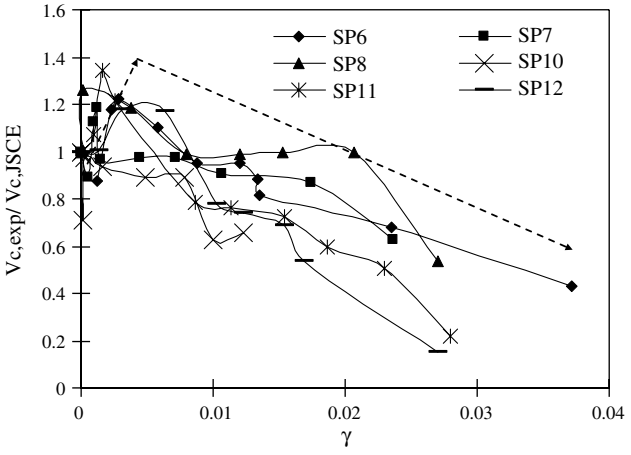

Fig. 14. Concrete strength reduction versus shear deformation ratio.

the issue of how to predict shear deformation and model the change in the potential shear capacity during the development of flexural deformation seems to be important, since large shear deformation at the hinge zone causes deterioration of the concrete contribution to shear, and consequently affects ductility development. This will be a task to the future, to follow the present study.

3.4.3. Drift ratio due to bending

In this paper, deformation due to bending is separated into two parts: the elastic flexural bending component and the plastic component. The conventional moment-curvature method can be used to predict the elastic flexural bending component before the steel yielding. For simplicity, elastic flexural displacement is calculated from Euler's beam theory in which Branson's equation for the effective moment of inertia is applied

$$\delta_f = \frac{VL^3}{3E_cI_e} \tag{6}$$

where V is applied shear force, E_c is Young's modulus of concrete, L is shear span, and I_e is the effective moment of inertia according to Branson [17], which can be calculated as follows:

$$I_e = I_g\left(\frac{M_{cr}}{M_{max}}\right)^3 + I_{cr}\left\{1 - \left(\frac{M_{cr}}{M_{max}}\right)^3\right\} \tag{7}$$

where

I_g	moment of inertia of concrete gross
I_{cr}	moment of inertia of cracked concrete
M_{cr}	cracking moment
M_{max}	maximum moment

Fig. 15(a) shows the comparison of yield deformation from the experiment and from the analytical formula. Yield deformation from the analysis is considered as a summation of pullout deformation calculated using Eqs. (1)–(5), and elastic flexural deformation using Eqs. (6) and (7). The analytical result shows a smaller value compared to the experimental result because the pull out deformation equation is somewhat conservative.

After the yielding of the longitudinal reinforcement, deformation due to rotation within the plastic hinge dominates the total displacement of the piers. Plastic flexural deformation is back-calculated by subtracting the elastic flexural deformation, deformation due to pullout, and shear deformation from the total deformation in the experiment. The rotation due to plastic deformation (θ_p) can be calculated using Eq. (8)

$$\delta_p = \theta_p \cdot \left(L - \frac{L_p}{2}\right) \tag{8}$$

where

L	shear span
L_p	plastic hinge length

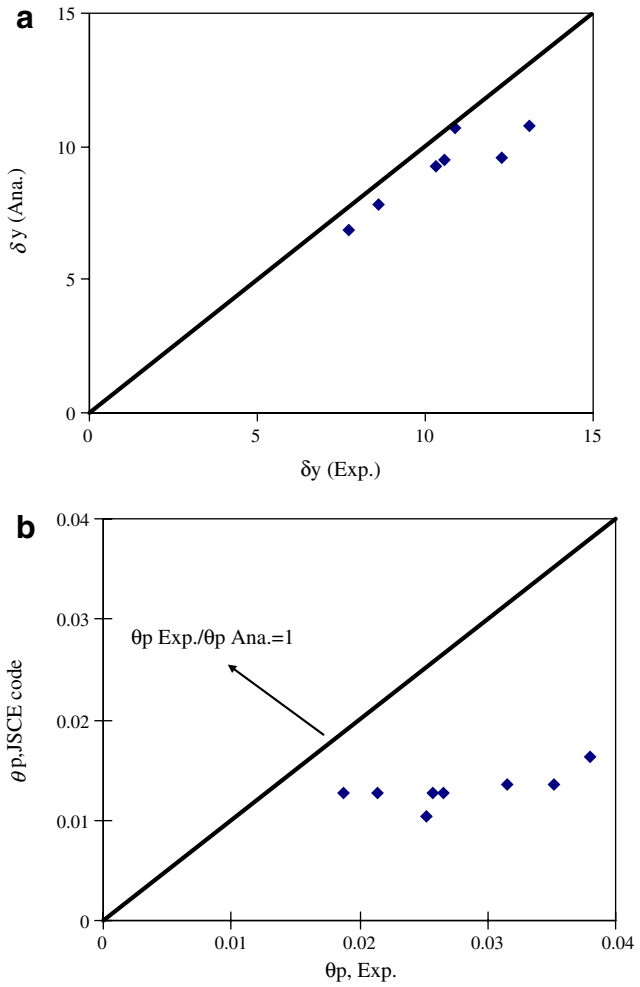

Fig. 15. Flexural deformation. (a) Yielding displacement, (b) plastic drift ratio at the maximum load.

θ_p rotation due to plastic deformation
δ_p plastic deformation

The plastic rotation at the maximum load before the decrease of load-carrying capacity from the experiment was compared to that calculated by Eq. (9), which is the equation for plastic rotation for unstrengthened RC structures calculated from JSCE [15]. This equation suggests that the maximum plastic rotation depends on the ratio of shear and longitudinal reinforcement. Fig. 15(b) shows that the present JSCE code [15] gives a conservative prediction for the plastic rotation of RC piers strengthened with PET fiber.

$$\theta_{mp} = \frac{0.021 k_s \cdot \rho_w + 0.013}{0.79\rho_t + 0.153} \quad (9)$$

where
θ_{mp} plastic rotation at the maximum load
k_s factor to consider the strength of lateral re-bars
ρ_w lateral reinforcement ratio (%)
ρ_t tensile reinforcement ratio (%)

To reflect the strengthening effects of large fracturing strain FRP materials, a new factor K_0 is introduced in the modeling and calculated from experimental results as follows:

$$K_0 = \frac{\theta_{mp}(0.79\rho_t + 0.153) - 0.013}{0.021 k_s \rho_w} \quad (10)$$

The experimental relationships between K_0 and $E_{frp}\rho_{frp}$ are plotted in Fig. 16(a). It is indicated that K_0 increases with the $E_{frp}\rho_{frp}$ meaning the plastic rotation at the maximum load increases with the tensile stiffness of the FRP provided for confinement. An empirical formulation (11) can be given, as follows, to K_0 through linear regressing

$$K_0 = 0.0019 E_{frp} \cdot \rho_{frp} + 3.65 \quad (11)$$

Therefore a modified formulation based on the JSCE for predicting the plastic rotation of RC piers strengthened with large fracture strain FRP can be written as follows:

$$\theta_{mp} = \frac{0.021 k_s K_0 \rho_w + 0.013}{0.79\rho_t + 0.153} \quad (12)$$

where, K_0 is the factor representing fiber confinement

The comparison between the analytical prediction and the experimental result is shown in Fig. 16(b). By giving a factor

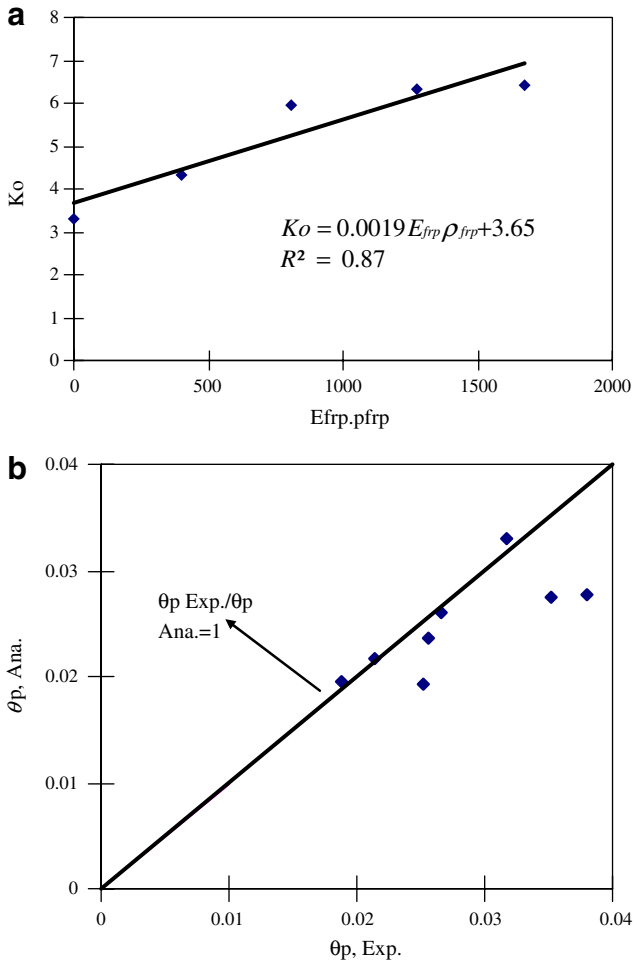

Fig. 16. Plastic rotation. (a) Relation of K_0 and $E_{frp}\rho_{frp}$, (b) plastic rotation comparison of analysis and experimental results.

K_0 as a function of fiber confinement stiffness, the plastic rotation of strengthened RC piers using PET fiber can be predicted with reasonable accuracy. As Fig. 16(a) shows, plastic rotation can be improved by a higher fiber ratio.

4. Prediction of drift ratio at the ultimate state

It is difficult to distinguish all deformation components in the descending part beyond point M in Fig. 9 due to the breakage of the strain gauges and the instability of the testing instruments. The assumption is that the descending slope of load-carrying capacity is of a linear decreasing rate, which is proposed by JSCE [15] for practical design use, applied here as follows:

$$\theta_u = \theta_m + \eta\left(1 - \frac{M_u}{M_{max}}\right) \tag{13}$$

where

θ_u	total drift ratio at ultimate state
θ_m	total drift ratio at maximum load
M_u	ultimate moment which can be considered as same value of yield moment
M_{max}	moment at peak load
η	factor to consider the gradient of linear softening of members

It can be clearly seen in Fig. 7 that the FRP confinement ratio does not only influence the starting points of the descending parts but also influences the descending slope η in the P–δ envelope curves. Fig. 17(a) shows the relationship between η and strengthening fiber ratios, K_u. It can be inferred that the initial ratios of shear to flexural capacity of the piers before strengthening, and the strengthening ratio, are influential upon ductility. A comprehensive parameter K_u is introduced

$$K_u = \frac{V_w + V_c}{V_{mu}} \cdot \frac{E_{frp} \cdot \rho_{frp}}{E_w \cdot \rho_w} \tag{14}$$

where the first and second parts represent the nature of the RC piers before strengthening and the strengthening ratio, respectively. By regression, the following equation to predict the descending part can be obtained:

$$\eta = 1.22K_u + 0.04 \tag{15}$$

where

η	factor to consider the gradient of linear softening of members
V_w	contribution of steel shear reinforcement
V_c	concrete shear contribution predicted by JSCE
V_{mu}	shear force corresponding to flexural capacity
E_{frp}	modulus elasticity of FRP
ρ_{frp}	FRP ratio (%)
E_w	modulus elasticity of steel shear reinforcement
ρ_w	steel shear reinforcement ratio (%)

By using this equation and the models for predicting the drift ratio at the maximum load, the ultimate deformation of strengthened RC piers can be predicted for practical design use. Fig. 17(b) provides a comparison between the experimental results and the analytical ones. It is apparent that the modeling for ultimate deformation presents rather good accuracy.

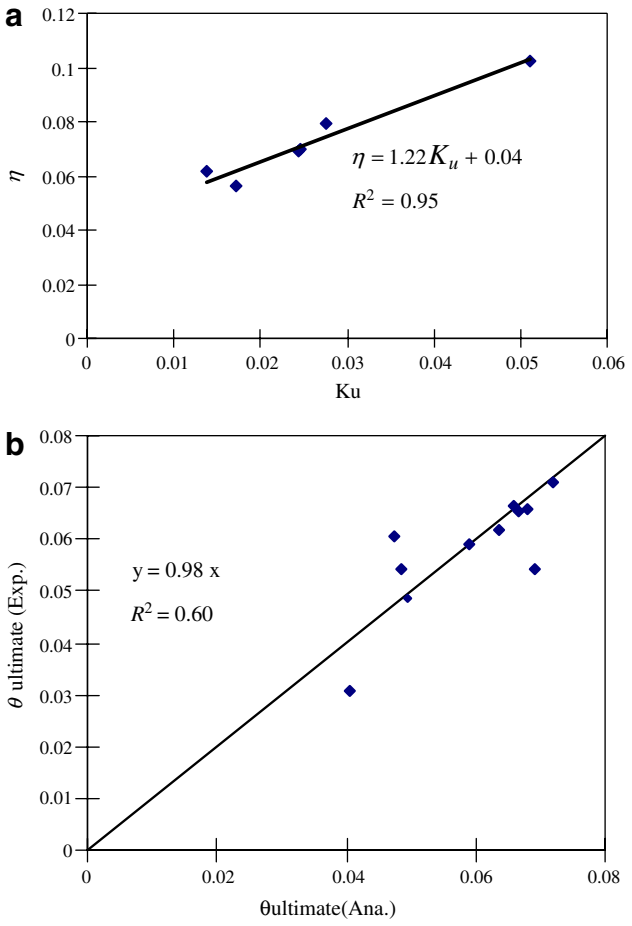

Fig. 17. Ultimate rotation. (a) Relation of η and $\frac{V_s}{V_{mu}} \cdot \frac{E_{frp}\rho_{frp}}{E_s\rho_s}$, (b) ultimate rotation comparison of analysis and experimental results.

5. Conclusions

Experiments were performed in order to determine the effectiveness of new fiber materials, polyethylene terephthalate (PET) and polyethylene naphthalate (PEN), which have low stiffness and high fracturing strain profile, as externally wrapped shear reinforcement. From the experiments, the following conclusions were obtained:

- RC piers wrapped by PET and PEN fiber sheets with large fracturing strain could efficiently enhance the ductility of reinforced concrete (RC) piers regardless of their low stiffness. The large fracturing strain allowed the fiber to contribute sufficient shear force at the ultimate state while avoiding fiber rupture.
- PET and PEN can be used for shear strengthening of RC piers lacking transverse reinforcement if an adequate amount of fiber is provided, despite their low

stiffness. However, for RC piers that are heavily insufficient in shear capacity, it might be less cost effective to use PET and PEN since a large amount of fiber is necessary.

- The strain development of both externally bonded fiber sheets and internally placed steel shear reinforcements are rather similar in RC piers wrapped with fiber sheets.
- Debonding of fiber tends to occur early in RC piers deficient in shear due to large stress concentration along the crack area of the concrete.
- Shear deformation of RC piers wrapped with FRP sheets increases with the increase in shear contribution by shear reinforcement (fiber sheets and steel ties in this study) and increases rapidly after yielding of the steel shear reinforcement.
- At the same level of strain development in externally wrapped fiber, larger shear deformation occurs for piers with a high fiber ratio. As result, the shear deformation at the hinge zones causes a deterioration of the concrete contribution to shear and affects ductility development. Modeling the change of shear capacity during the development in flexural deformation is necessary.
- A concept for determining the characteristic P–δ curves of RC piers strengthened with large fracture strain FRP materials – PEN and PET – is proposed. The present JSCE seismic design equation proposed for RC piers underestimates the pullout deformation and the plastic flexural rotation at the starting point of the descending parts of P–δ curves of FRP strengthened RC piers. Hence new formulations are put forward and verified by experimental results.
- Formula for predicting the ultimate deformation of RC piers strengthened with large fracture strain FRP materials are proposed and show acceptable accuracy in comparison to the experimental results.

Acknowledgements

The fiber sheet material and experimental program was sponsored by the Aramid Retrofitting System Association as part of an effort to develop new fiber material for seismic strengthening. The major part of the experimental work was carried out at Mitsui-Sumitomo Research Institute in Tochigi. The assistance from the technical staff there is greatly appreciated.

References

[1] Triantafillou TC. "Seismic retrofitting using externally bonded fibre reinforced polymers (FRP)" fib courses, Athens, 4–5 May 2003.

[2] Monti G. Seismic upgrade of reinforced concrete columns with FRP, Teheran, 22 July 2003.

[3] Sheikh SA, Yau G. Seismic behaviour of concrete columns confined with steel and fiber-reinforced polymers. ACI J 2002;99(1): 72–80.

[4] Iacobucci RD, Sheikh SA, Bayrak O. Retrofit of square concrete columns with carbon fiber-reinforced polymers for seismic resistance. ACI J 2003;100(6):785–94.

[5] Nigel Priestley MJ, Seible Frieder, Xiao Yan, Verma Ravindra. Steel jacket retrofitting of reinforced concrete bridge columns for enhanced shear strength – Part 1: Theoretical considerations and test design. ACI J 1994;91(4):394–405.

[6] Nigel Priestley MJ, Seible Frieder, Xiao Yan, Verma Ravindra. Steel jacket retrofitting of reinforced concrete bridge columns for enhanced shear strength – Part 1: Test result and comparison with theory. ACI J 1994;91(5):537–51.

[7] Sirbu G. Resisting shear capacity of a reinforced concrete pier retrofitted with carbon fiber sheet, Master thesis, Hokkaido University, March 1998.

[8] Khalifa A, Gold WJ, Nanni A, Aziz MIA. Contribution of externally bonded FRP to shear capacity of flexural members. ASCE J Compos Construct 1998;2(4):195–203.

[9] Tuladhar R, Utsunomiya T, Ueda T. New flexible system of transverse reinforcement for RC piers. Adv Struct Eng 2003;6(3):216–30.

[10] Jaqin H, Nakai H, Ueda T, Sato Y, Dai J. Seismic retrofitting of RC piers using continuous fiber sheet with large fracturing strain. J Struct Eng (JSCE) 2005;51A(March):893–902.

[11] Ueda T, Sato H, Anggawidjaja D, Nakai H. Seismic retrofit by continuous fiber sheet with large fracturing strain. In: Composites in construction 2005 – Third international conference, Lyon, France, July 11–13, 2005.

[12] JSCE 292 Committee on Concrete Structures with Externally Bonded Continuous Fiber Reinforcing Materials, Recommendation for upgrading concrete structures with use of continuous fiber sheets, Concrete Engineering Series 41, JSCE, 2001.

[13] Ishibashi T, Tsuyoshi T, Kobayashi K, Yoshida T, Umihara T. Study on ductility evaluations on reinforced concrete columns subjected to reversed cyclic loading with large deformations. In: Proceedings of JSCE, No. 711/V-56, August 2002. p. 79–96.

[14] Shima H, Chou L, Okamura H. Micro and macro models for bond in reinforced concrete. J Faculty Eng, The University of Tokyo (B) 1987;XXXIX(2):133–94.

[15] JSCE Subcommittee on English Translation of the Standard Specifications, Standard specifications for concrete structures – 2002 'Seismic Performance Verification', JSCE Guidelines for Concrete, JSCE, No. 5, March 2005.

[16] Ueda T, Sato Y, Ito T, Nishizono K. Shear deformation of reinforced concrete beam, JSCE J Mater, Concrete Structures, Pavements, No 711/V-56, August 2002. p. 205–15.

[17] ACI 318, 2002, Building code requirements for structural concrete (ACI 318-02) and commentary (ACI318R-02), ACI Committee 318, Farmington Hills, MI, USA. p. 443.